Supplementary Information to

Grain Size Influences Activation Energy and Migration Pathways in $MAPbBr_3$ Perovskite Solar Cells

Lucie McGovern, Isabel Koschany, Gianluca Grimaldi, Loreta A. Muscarella, Bruno Ehrler

Center for Nanophotonics, AMOLF, Science Park 104, 1098 XG Amsterdam, The Netherlands

Section S1: Device Fabrication and Characterization

The solar cell fabrication closely follows the recipes established in Reference [1], with the notable exception of the $MAPbBr_3$ perovskite layer preparation, which we detail below.

The precursor for the $MAPbBr_3$ layer is fabricated from two solutions dissolved together in dimethyl sulfoxide (DMSO). First, a solution of 5.5 M methylamine hydro bromide (MABr, TCI) is made by dissolving the powder in DMSO (Sigma-Aldrich). To ensure a complete dissolution, the precursor is stirred and heated on a hot plate to 50-60°C. The second precursor is a 1.8 M lead(II) acetate trihydrate (PbOAc) solution (Sigma-Aldrich). To prepare this solution, the PbOAc powder is dissolved in DMSO and stirred and heated to 50-60°C overnight. Both precursor solutions are stirred and heated up to 65°C until a clear dense solution is formed. This final $MAPbBr_3$ precursor solution has a molarity of 3.05 M. For the spin coating step, 200 µL are used per sample, with a spin coating speed of 7500 rpm. To vary the grain size in the perovskite film, we vary the spin coating times: 5 s, 10 s, 20 s and 60 s. The samples are annealed for 1 h on the hot plate at 70 °C. During this annealing step, the samples quickly show a yellow-orange color, characteristic for $MAPbBr_3$. All of the above steps are carried inside a glovebox in a nitrogen atmosphere, with an O_2 level below 1 ppm.

For proper investigation both of the perovskite layer and of the full device, cells are either prepared until the perovskite layer (optical microscopy and EBSD imaging) or as the whole device (all electrical measurements and SEM cross-section imaging).

Optical microscopy images are taken using a Imager.A2m Zeiss microscope with an AxioCam ICc 5 camera in the dark field mode, with magnification objectives of x20, x50 or x100. Many images of the various samples are collected and the evaluation of each grain size is done through software evaluation using the program ImageJ. Specifically, to characterize the polydispersity in grain size, we take OM pictures at multiple spots and of multiple films spin coated for the same duration. For each of these images we measure the average grain size. Performed over multiple images, we obtain statistics on the grain size distribution for about 60 to 80 grains per spin coating condition. We note that the word “grain size” used in the main text and in the present SI systematically refer to grain diameter.

The SEM images are taken with a FEI Verios 460 scanning electron microscope in the secondary electron mode. The sample is cleaved in the center to obtain the cross-section image. The acceleration voltage used is of 10 kV and the working distance of 4 mm. EBSD images of $MAPbBr_3$ on NiO_x are collected by using a direct electron detector based on the Timepix sensor from Amsterdam Scientific Instruments (ASI). The best parameters for the scans are found to be 10 keV for the voltage, 100 pA for the current, 50 ms for the exposure time, and between 10 and 12 mm for the working distances. The step size is chosen depending on the cluster size shown by the specific sample. EBSD data are collected using EDAX OIM software, and a Python script is used for image processing. The resulting Kikuchi patterns are indexed using cubic symmetry, using 1−3° as the degree of tolerance.

Characterizing the $MAPbBr_3$ layer after different spinning durations, we notice, on top of the grain size evolution, an evolution in the thickness of the perovskite layer. Samples prepared after 5 or 10 seconds spinning duration have a thickness of 310 ± 10 nm, while the samples prepared after 20 or 60 seconds spinning duration have a thickness of 215 ± 10 nm. This thickness difference is incorporated into the different equations presented in Section 2 below.

The solar cell performance of the devices fabricated using the polycrystalline $MAPbBr_3$ perovskite layer of variable grain size is investigated below. The IV characteristics from the best cells are shown in Figure S1a, where it is already apparent that the FF and J_{SC} are the values most affected by grain size. For a fairer comparison, the average values taken over multiple pixels from multiple devices are shown in Table 1.

The V_{OC} does not change as a function of grain size, which is an indication that the amount of non-radiative recombination is similar in all devices. More details on this topic are provided in Section 4 below.

The overall PCE of the devices is constant through the series of varying grain size films: from 1% to 1.3%. The devices show reasonable efficiency for the simplistic solar cell architecture considered here which is in line with other works using similar HTL and ETL[2]. As mentioned in the main text, we choose the extraction layers NiO_x, C_{60} and BCP mainly because they are not themselves affected by ion migration, contrary to other commonly used extraction layers such as Li-TFSI doped Spiro-O-meTAD[3,4]. We note that the low efficiency does not affect the TID measurement. The devices are measured in the dark where the measurement mainly requires a low dark current to avoid electrical charge flowing through the device affecting the depletion layer width.

Two parameters are affected by grain size, J_{SC} and FF, in an opposing manner, where the increase of one is concomitant to the decrease of the other – thereby maintaining a constant PCE. The relatively low fill factor values are partly due to a low shunt resistance. As mentioned earlier, this can be modulated by further device engineering and is therefore not the focus of the present study.

The EQE curves of the devices in Figure S1b match well with the corresponding IV curves of Figure S1a, with slightly lower J_{SC} values showing as lower EQE values. The highest EQE point reaches almost 60 %, for the sample spin coated for 60 seconds (i.e. with smallest grain size). The overall shape of the EQE feature follows that of typical $MAPbBr_3$ absorption, with the characteristic excitonic peak at 525 nm, and the relevant bandgap at 540 nm.

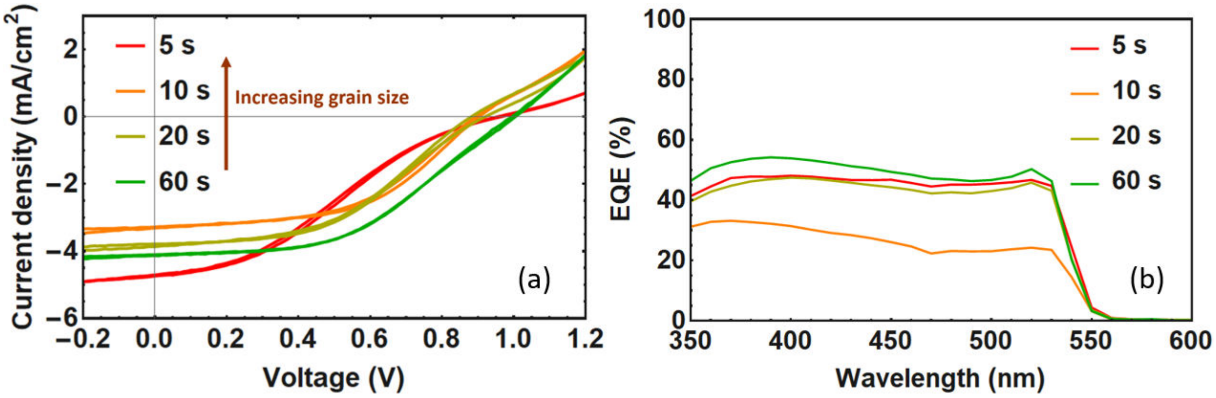

Figure S1: (a) Light IV curves of the best pixel for each of the solar cell device made with a photoactive layer of polycrystalline $MAPbBr_3$, spin coated for 5, 10, 20 or 60 s, and (b) the corresponding EQE curves.

Table 1 : Average IV solar cell charasteristics of the devices made with a polycrystalline $MAPbBr_3$ film prepared with a spin coating process of 5, 10, 20 or 60 s.

	5 s	10 s	20 s	60 s
J_{SC} (mA/cm^2)	4.1 ± 0.2	3.20 ± 0.06	3.6 ± 0.2	4.3 ± 0.3
V_{OC} (V)	0.88 ± 0.03	0.84 ± 0.02	0.87 ± 0.02	0.82 ± 0.024
FF (%)	27.4 ± 2.7	47 ± 1.5	39.2 ± 1.7	36 ± 2.2
PCE (%)	1.0 ± 0.1	1.3 ± 0.06	1.2 ± 0.1	1.3 ± 0.14

Section S2: Capacitance Measurements

For TID measurements the sample is loaded into a Janis VPF-100 liquid nitrogen cryostat inside a nitrogen-filled glovebox. Impedance spectroscopy, capacitance-voltage, transient ion-drift and deep level transient spectroscopy measurements are performed at a pressure below 2 x 10- 6 mbar, in the dark, using a commercially available DLTS system from Semetrol. To ensure thermal equilibrium, the temperature of the sample is held constant for at least 30 minutes before impedance spectroscopy and capacitance-voltage measurements. Capacitance transient measurements were performed from 210 K to 330 K in steps of 3 K with a temperature accuracy of 0.2 K. The sample is held at 210 K for 30 minutes before starting the transient ion-drift and deep level transient spectroscopy measurements.

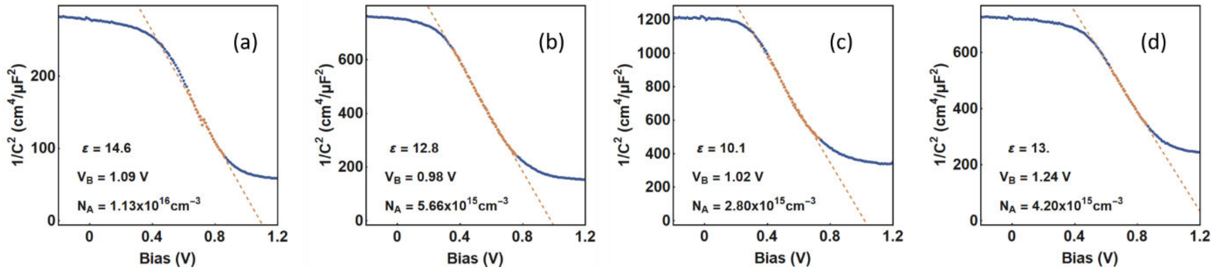

Figure S2: Mott-Schottky plots of the devices with $MAPbBr_3$ perovskite films of (a) 1.7 µm grain size; (b) 1.9 µm grain size; (c) 4.8 µm grain size; (d) 11.3 µm grain size.

TID is a technique which makes use of a voltage bias to redistribute ions within a device. The voltage applied should thus be close to the built-in voltage of the cell. We determine this value by Mott-Schottky analysis[5] as shown in Figure S2. We obtain values of 1.09 V, 0.98 V, 1.02 V and 1.24 V for typical devices with grain size 1.7 µm, 1.9 µm, 4.8 µm and 11.3 µm, respectively. In the subsequent TID measurements, we thus apply voltage biases of 1 V (see Figure 2 of the main text) and 1.1 V (see Figure S3). We further measure the devices with a lower applied voltage of 0.75 V in order to test the measurement response and to check if ion migration is already visible for smaller built-in fields. We note that our Mott-Schottky measurement is taken in reverse mode, and that the doping density values are found to be above the minimal threshold for correct Mott-Schottky evaluation[6].

The steady-state capacitance (determined either by Thermal Admittance Spectroscopy (TAS) or by TID, taking the values at longer times) is found to be stable with temperature (see Fig. S3 below). We attribute this effect to the choice of contact layers, NiO_x and C_{60}. Indeed, if we chose other contact layers, the geometric capacitance would become temperature dependent, presumably because of the formation of a dipole layer at that interface[7].

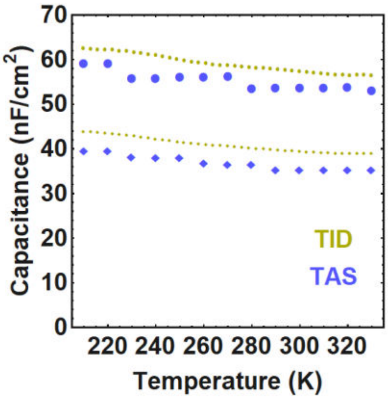

Figure S3: Steady-state capacitance values obtained by thermal admittance spectroscopy measurements at 10 kHz - in green – and from TID measurements, taking the capacitance value at longer times - in blue - for the cells with small and large grain size (represented by circle and diamond respectively).

As discussed in the main text, the extraction layers are chosen specifically because they exhibit no direct ion migration, even though they may reduce the overall PCE of the devices. Ion migration through the extraction layers into the contact layers may still happen on long timescales[8].

In Figure S4 (a) - (h) we show the TID traces taken at different filling voltages of 0.75 V and 1.1 V, for the samples from the smallest (Figure S4 a, e) to the largest grain size (Figure S4 d, h). The first observation is the presence of a similar trend in all cases, that is that the capacitance decreases with time. This pattern is conserved for the samples with small and large grain size, and for all filling voltages. The ion migration process at play must therefore remain bromide migration.

One parameter is, however, affected by the voltage pulse: the height of the transient, with higher voltages leading to a more pronounced transient. This indicates a difference in the density of mobile ions measured after applying the different filling voltages: more bromide mobile ions have been displaced when applying a voltage pulse of 1 V or 1.1 V, rather than a lower voltage pulse of 0.75 V. Some but not all of the mobile bromide ions in our devices have thus already been displaced by a voltage pulse of 0.75 V. This trend is consistent with a built-in voltage of about 1 V, meaning that the device is still partially depleted at 0.75 V.

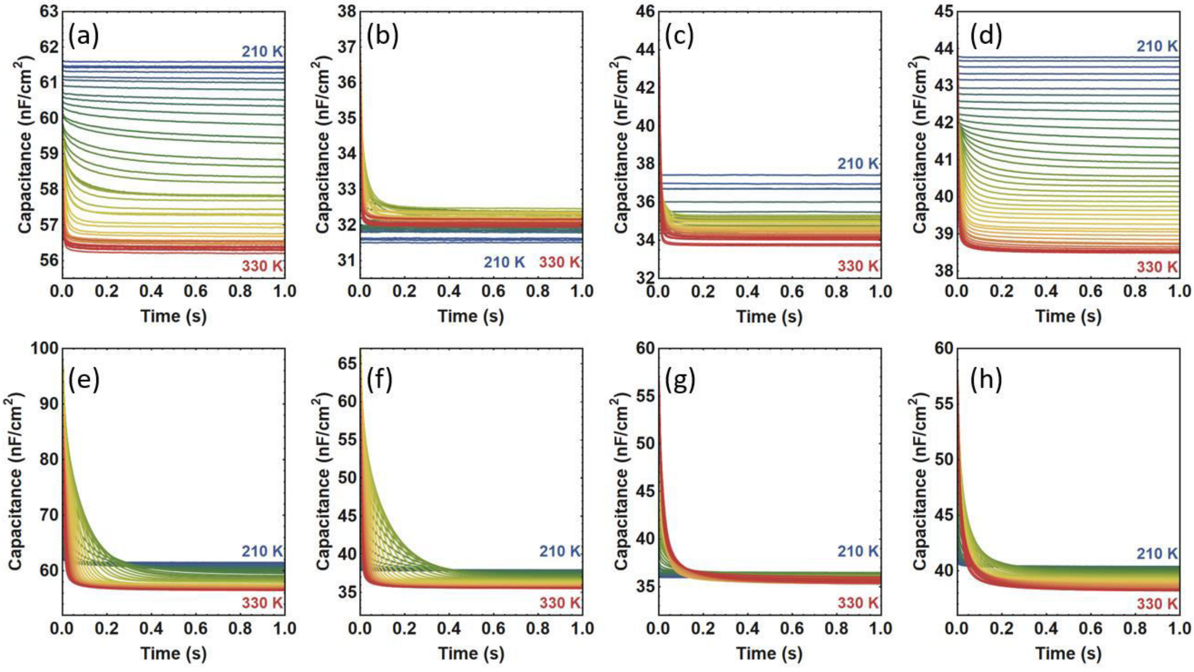

Figure S4: TID traces measured after applying filling voltage of 0.75 V for 2 seconds to the devices with $MAPbBr_3$ perovskite films of (a) 1.7 µm grain size; (b) 1.9 µm grain size; (c) 4.8 µm grain size; (d) 11.3 µm grain size; TID traces measured after applying a filling voltage of 1.1 V for 2 seconds to the devices with $MAPbBr_3$ perovskite films of (e) 1.7 µm grain size; (f) 1.9 µm grain size; (g) 4.8 µm grain size; (h) 11.3 µm grain size.

To quantify bromide migration, we use a global fit algorithm. The fit function is the following:

$$C(t,T) = C_{\infty}(T) + \Delta C(T)\exp\left(\frac{-t}{p_{fit}\,T\exp\left(\frac{E_a}{k_B T}\right)}\right)$$

where $C(t,T)$ is the capacitance as a function of time and temperature, $C_{\infty}(T)$ is the steady-state value of the capacitance at a certain temperature T, $\Delta C(T)$ is the height of the transient at temperature T, p_{fit} is a fitted parameter and E_a is the activation energy of the process. This fit function can be further extended with any number of additional exponential terms if needed, each with their own $\Delta C_{(n)}$, $p_{fit\,(n)}$ and $E_{a(n)}$. The fitting procedure goes as follows: $C_{\infty}(T)$ is extracted from the measurements directly from the steady-state capacitance before we allow the algorithm to find the best value for $\Delta C(T)$ at each temperature and the best global values for p_{fit} and E_a. We thus directly obtain the value of the activation energy E_a, and further convert p_{fit} and $\Delta C(T)$ into diffusion coefficient and density of mobile ions.

The conversion of p_{fit} and $\Delta C(T)$ to diffusion coefficient and density of mobile ions is described below. For diffusion coefficient determination, we first calculate the temperature-independent diffusion prefactor D_0 using the following equation[9]:

$$D_0 = \frac{k_B\,\varepsilon\,\varepsilon_0}{q^2\,N_A\,p_{fit}}$$

where k_B is the Boltzmann constant, ε is the perovskite permittivity, ε_0 is the vacuum permittivity, q is the elementary charge, N_A is the doping density and p_{fit} the value obtained through the fitting algorithm. Now, D_0 can be used to calculate the diffusion coefficient $D(T)$ at a given temperature:

$$D(T) = D_0 \exp\left(\frac{-E_a}{k_B\,T}\right)$$

where E_a is the activation energy extracted from the fit. In Figure 3b we present the diffusion coefficients calculated at room temperature, $D(298\,K)$.

The ion concentration N_{ion} can be determined from the fitted $\Delta C(T)$ parameter by the equation[9]:

$$N_{ion}(T) = 2\, N_A\, \frac{\Delta C(T)}{C_\infty(T)}$$

where $\Delta C(T)$ is the value obtained at each temperature through the fitting algorithm. In Figure 3c, we present the maximal value for the density of mobile ions, N_{ion} (max).

To apply these conversions from p_{fit} and $\Delta C(T)$ to $D(T)$ and $N_{ion}(T)$, we need values for the perovskite permittivity ε and for the doping density N_A of the devices. These are determined through Mott-Schottky analysis, as shown in Figure S2. For typical devices made with small (large) grain size, the perovskite permittivity is of 14.6 (13), while the doping density reaches 1.13x10^{16} (4.2x10^{15} cm^{-3}).

To write the previous set of equations, several assumptions are necessary. We first assume that the electric field is mostly determined by the doping density, and that the ions only pose a small perturbation, i.e. that the depletion width is mostly governed by the electronic charge carriers, and only slightly affected by the migration of ions. We further make three assumptions: first, that the electric field after application of the voltage pulse varies linearly within the perovskite bulk[10,11]; second, that the total ion density is conserved; and third, that the diffusion is negligible against drift.

While fitting the capacitance transients, we find that a biexponential fit works well to describe the data, which supports the hypothesis of two specific ionic contributions, rather than a broad distribution of a single peak[12]. Within each of these migration pathways, however, we cannot completely exclude some distribution in the activation energy and/or diffusion coefficient.

Looking at the results in Figure 3 of the main text, we note that we would expect a reduced diffusion coefficient when the activation energy increases if nothing else changes, contrary to our observation. If we expand the full equation for the diffusion coefficient D_{ion}, we find:

$$D_{ion} = \frac{v_a d^2}{6}\, exp\left(\frac{\Delta S}{k_B}\right)\, exp\left(-\frac{\Delta H}{k_B T}\right)$$

with v_a the attempt frequency for the ionic jump, d the ionic jump distance, ΔS and ΔH the changes in Gibbs free entropy and enthalpy of activation for a single ion migration step[9].

The combination of an increased activation energy with a constant diffusion coefficient suggests a compensating term when the average grain size is increased: this could be either an increase in the attempt frequency v_a, an increase in the ionic jump distance d, or an increase in the entropy term ΔS. Regarding the first hypothesis, the presence of uncoordinated atoms in the grain boundary region suggests weaker bonding of the perovskite lattice at these grain boundaries, which is generally related to lower attempt-to-escape frequencies. This would lead indeed to an increase of v_a with grain size. If we consider the ionic jump distance d, and follow our previous statement that the defect formation energy is independent with grain size, then d should remain constant with grain size. On the other hand, at grain boundaries, the higher degrees of freedom suggest that ΔS should increase with the amount of grain boundaries, i.e. the trend would consist of a decrease of ΔS with grain size. Together, these suggest that the compensating term is an increase of the attempt to escape frequency v_a.

Section S3: Model of Ion Migration Pathways

The scheme of migration pathways presented in Figure 4 of the main text can be further used to estimate key parameters in the bromide migration process at play. Indeed, from the activation energies of peak A in Figure 3 of the main text, we can recover the two underlying activation energies needed for the migration from bulk to grain boundaries, and from grain boundaries to the electrode.

To do so, we use a geometric model as shown in Figure S5. Any given bromide ion will travel a distance $L1$ inside the bulk, then $L2$ through the grain boundary, here represented as the edge of the rectangle. If the ion starts in position (x, y), where x is the distance between the ion and the electrode in the vertical plane, and y is the distance between ion and grain boundary in the horizontal plane, the fraction f of bulk travelling distance to total travelling distance, i.e. $f = \frac{L1}{L1+L2}$ is equal to the following expression:

$$f[v1, v2, L, H] = \frac{\int_0^{x_{max}} dx \int_{x\frac{\sqrt{v2^2-v1^2}}{v2-v1}}^{H} dy \frac{1}{1-\frac{v1}{v2}+\frac{y}{x}\sqrt{1-\left(\frac{v1}{v2}\right)^2}}}{\int_0^{x_{max}} dx \int_{x\frac{\sqrt{v2^2-v1^2}}{v2-v1}}^{H} dy}$$

With distances as defined in Figure S5 and x_{max} the minimal value between $x_{max} = \frac{L}{2}$ and $x_{max} = \frac{H\,(v2-v1)}{\sqrt{v2^2-v1^2}}$.

The expression for f thus takes into account all possible starting values for (x, y).

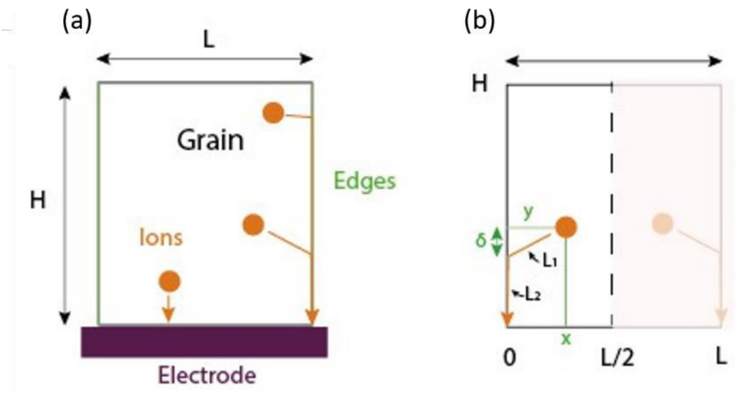

Figure S5: (a) Geometric scheme showing bromide ions within a perovskite grain for a grain of height H and length L, on top of an electrode. The inside of the rectangle represents the bulk of the perovskite lattice, while the edges of the rectangle represent grain boundaries. (b) Mean free path from the grain interior to the electrode of opposite polarity of an ion located at position (x,y), with $L = L1 + L2$, $L1$ being the distance from grain interior to grain boundary, and $L2$ from grain boundary to electrode.

The effective activation energy of peak A, $E_{a(eff)}(A)$ can be written as

$$E_{a(eff)}(A) = f\ E_a(1) + (1 - f)\ E_a(2)$$

where $E_a(1)$ and $E_a(2)$ are the bromide migration activation energies from bulk to grain boundary and from grain boundary to electrode, respectively, where the conversion relation from $v1$ to $E_a(1)$, and from $v2$ to $E_a(2)$ are $v1 = Exp[-E_a(1)]$ and $v2 = Exp[-E_a(2)]$. We note that this simplification assumes that the diffusion coefficient for both pathways is identical and only the activation energy is different, as also indicated by our measurement (Figure 3d of the main text).

We can now estimate $E_a(1)$ and $E_a(2)$, by solving the previous equation for various sets of $(E_a(1), E_a(2))$ and try to find the best fit to the activation energies of peak A. The results are shown in Figure 4c of the main text. We note that the x-axis for activation energies of peak A (as shown in Figure 3c of the main text) is transformed from grain size to a new metric of grain size over thickness of the perovskite layer, allowing to plot all experimental values on the same axis as the fitted values. The simple model we used predicts a change in the activation energy for aspect ratios between 0 and 2, while our experimental data shows an onset starting around 7,8. The failure to account for the delayed onset of the activation energy change is likely due to the simplicity of our model, which does not account for the distribution of grain sizes in each sample, a possibly rough grain boundary, and for the contribution of a slower diffusion paths to the capacitance decay. Nevertheless, if we shift the x-axis of the model by 7.8, we can reproduce the trend of the activation energy increase as a function of grain aspect-ratio. The plot in Figure 4c of the main text was obtained with fitted values of the activation energies of 0.50 eV for bulk diffusion and 0.18 eV for grain-boundary diffusion. While not attempting a precise description of the experimental data our model shows the effect that a varying grain size has on the geometry of the ion's path, rationalizing the experimental trend.

We further note that TID cannot unveil the microscopic pathways of ion diffusion in the perovskite layer, but remains an interesting tool that can be further complimented by theoretical modelling using DFT and MD simulations.

Section S4: Trap states

The vacancies necessary for ion migration to occur are part of the wider range of traps and charged point defects that hybrid halide perovskites exhibit[13].

We can study this trap behavior using a deep level transient spectroscopy (DLTS) measurement. DLTS is similar than TID, only the duration of the voltage pulse is shorter, such that traps have enough time to be filled, but ions do not have sufficient time to diffuse[9]. This technique has been extensively used in the past to measure trap state energy and density[14].

Here we apply a filling pulse of 1 V for a duration of 20 ms to the cells with smallest and largest grain size. The resulting transients are fitted with a global fit procedure, analogous to the one presented for TID.

The fitting function has the same form as in equation 1 of the main text,

$$C(t,T) = C_{\infty}(T) + \Delta C(T)\,\exp\left(\frac{-t}{p_{fit}\,T\exp\left(\frac{E_T}{k_B T}\right)}\right)$$

with E_T the trap depth (replacing the activation energy E_a). The only difference lies in the conversion of the factor p_{fit} to the attempt frequency A_0 relevant for traps, where

$$A_0 = \frac{1}{p_{fit}\,T^3}$$

with A_0 the temperature-independent attempt frequency and the temperature-dependent attempt frequency $A(T) = A_0 T^2$.

The resulting trap depths, trap densities and trap attempt-to-escape frequencies of the $MAPbBr_3$ cells with smallest and largest grain size are presented in Table 2 below.

Table 2 : Average trap depth, density of traps and attempt frequency of the devices made with a polycrystalline $MAPbBr_3$ film prepared with a spin coating process of 5 or 60 seconds (respectively with largest and smallest grain size).

	5s (largest grains)	*60s (smallest grains)*
E_{trap} (eV)	0.192 ± 0.020	0.300 ± 0.002
N_{traps} (cm^{-3})	$(1.55 \pm 0.64) \times 10^{15}$	$(7.25 \pm 0.18) \times 10^{15}$
A(300 K) (s^{-1})	$(4.58 \pm 0.11) \times 10^{5}$	$(7.86 \pm 0.74) \times 10^{5}$

The cells made with $MAPbBr_3$ perovskite of smallest grain size have a trap depth of 300 meV, deeper than the 192 meV trap depth for the cells of largest grain size. This on its own could suggest an increase in the recombination rate for cells with smallest grain size. The density of traps is also highest for the cells with smallest grains, i.e. the cells with most grain boundaries. The factor of increase is a little over 4, close to the 3.8 difference in density of grain boundaries when going from cells with 1.7 µm grains to cells with 11.3 µm grains - this strongly suggests that the traps are located at the grain boundaries of the perovskite film.

Both trap density and trap depth thus suggest an increased recombination of electrons and holes for the cells with smallest grain size. On the other hand, the attempt frequency at room temperature A(300 K) is higher for the devices with smallest grain size, resulting in the following picture: the dense number of deep traps in cells with small grain size can counteract the higher attempt to escape frequency, thereby maintaining a constant level of non-radiative recombination in cells with small and large grain size. This is one possibility to explain the constant V_{OC} of the devices with respect to grain size (see Section S1). Another possibility is that the constant V_{OC} is a consequence of an interfacial energetic barrier between the perovskite and one of the transport layers, rather than by the recombination rate – the constant V_{OC} with regard to grain size would thus be linked to the materials' energetic offset.

Here we further confirm the observation of traps (and not ions) by the fact that the observed trend (energy decrease for cells with smallest grain size) is opposite to the one observed for ions with TID. From this analysis, it also follows that the density of mobile ions is not directly related to the density of traps in the perovskite layer.

References

(1) McGovern, L.; Futscher, M. H.; Muscarella, L. A.; Ehrler, B. Understanding the Stability of MAPbBr3versus MAPbI3: Suppression of Methylammonium Migration and Reduction of Halide Migration. *J. Phys. Chem. Lett.* **2020**, *11* (17), 7127–7132. https://doi.org/10.1021/acs.jpclett.0c01822.

(2) Hu, X.; Jiang, X. F.; Xing, X.; Nian, L.; Liu, X.; Huang, R.; Wang, K.; Yip, H. L.; Zhou, G. Wide-Bandgap Perovskite Solar Cells With Large Open-Circuit Voltage of 1653 MV Through Interfacial Engineering. *Sol. RRL* **2018**, *2* (8), 1800083. https://doi.org/10.1002/solr.201800083.

(3) Zhang, T.; Meng, X.; Bai, Y.; Xiao, S.; Hu, C.; Yang, Y.; Chen, H.; Yang, S. Profiling the Organic Cation-Dependent Degradation of Organolead Halide Perovskite Solar Cells. *J. Mater. Chem. A* **2017**, *5* (3), 1103–1111. https://doi.org/10.1039/C6TA09687E.

(4) Luo, Q.; Zhang, Y.; Liu, C.; Li, J.; Wang, N.; Lin, H. Iodide-Reduced Graphene Oxide with Dopant-Free Spiro-OMeTAD for Ambient Stable and High-Efficiency Perovskite Solar Cells. *J. Mater. Chem. A* **2015**, *3* (31), 15996–16004. https://doi.org/10.1039/c5ta02710a.

(5) Almora, O.; Aranda, C.; Mas-Marzá, E.; Garcia-Belmonte, G. On Mott-Schottky Analysis Interpretation of Capacitance Measurements in Organometal Perovskite Solar Cells. *Appl. Phys. Lett.* **2016**, *109* (17), 173903. https://doi.org/10.1063/1.4966127.

(6) Kirchartz, T.; Gong, W.; Hawks, S. A.; Agostinelli, T.; MacKenzie, R. C. I.; Yang, Y.; Nelson, J. Sensitivity of the Mott-Schottky Analysis in Organic Solar Cells. *J. Phys. Chem. C* **2012**, *116* (14), 7672–7680. https://doi.org/10.1021/jp300397f.

(7) Garcia-Belmonte, G.; Bisquert, J. Distinction between Capacitive and Noncapacitive Hysteretic Currents in Operation and Degradation of Perovskite Solar Cells. *ACS Energy Lett.* **2016**, *1* (4), 683–688. https://doi.org/10.1021/acsenergylett.6b00293.

(8) Kato, Y.; Ono, L. K.; Lee, M. V.; Wang, S.; Raga, S. R.; Qi, Y. Silver Iodide Formation in Methyl Ammonium Lead Iodide Perovskite Solar Cells with Silver Top Electrodes. *Adv. Mater. Interfaces* **2015**, *2* (13), 1500195. https://doi.org/10.1002/admi.201500195.

(9) Futscher, M. H.; Gangishetty, M. K.; Congreve, D. N.; Ehrler, B. Quantifying Mobile Ions and Electronic Defects in Perovskite-Based Devices with Temperature-Dependent Capacitance Measurements: Frequency vs Time Domain. *J. Chem. Phys.* **2020**, *152* (4), 044202. https://doi.org/10.1063/1.5132754.

(10) Birkhold, S. T.; T. Precht, J.; Liu, H.; Giridharagopal, R.; E. Eperon, G.; Schmidt-Mende, L.; Li, X.; S. Ginger, D. Interplay of Mobile Ions and Injected Carriers Creates Recombination Centers in Metal Halide Perovskites under Bias. *ACS Energy Lett.* **2018**, *3* (6), 1279–1286. https://doi.org/10.1021/acsenergylett.8b00505.

(11) Weber, S. A. L.; Hermes, I. M.; Turren-Cruz, S. H.; Gort, C.; Bergmann, V. W.; Gilson, L.; Hagfeldt, A.; Graetzel, M.; Tress, W.; Berger, R. How the Formation of Interfacial Charge Causes Hysteresis in Perovskite Solar Cells. *Energy Environ. Sci.* **2018**, *11* (9), 2404–2413. https://doi.org/10.1039/c8ee01447g.

(12) Reichert, S.; Flemming, J.; An, Q.; Vaynzof, Y.; Pietschmann, J.-F.; Deibel, C. Ionic-Defect Distribution Revealed by Improved Evaluation of Deep-Level Transient Spectroscopy on Perovskite Solar Cells. *Phys. Rev. Appl.* **2020**, *10*, 34018. https://doi.org/10.1103/PhysRevApplied.13.034018.

(13) Walsh, A.; Scanlon, D. O.; Chen, S.; Gong, X. G.; Wei, S.-H. Self-Regulation Mechanism for Charged Point Defects in Hybrid Halide Perovskites. *Angew. Chemie* **2015**, *127* (6), 1811–1814. https://doi.org/10.1002/ange.201409740.

(14) Johnson, N. M.; Bartelink, D. J.; Gold, R. B.; Gibbons, J. F. Constant-Capacitance DLTS Measurement of Defect-Density Profiles in Semiconductors. *J. Appl. Phys.* **1979**, *50* (7), 4828–4833. https://doi.org/10.1063/1.326546.